On sub-surface stress caused by contact roughness in compressible elastic solids

Murugesan, Yaswanth; Venugopalan, Syam P.; Nicola, Lucia

DOI
10.1016/j.triboint.2021.106867

Publication date
2021

Document Version
Final published version

Published in
Tribology International

Tribology International 159 (2021) 106867

Contents lists available at ScienceDirect

Tribology International

journal homepage: http://www.elsevier.com/locate/triboint

On sub-surface stress caused by contact roughness in compressible elastic solids

Yaswanth Murugesan [a], Syam P. Venugopalan [b], Lucia Nicola [a,b,*]

[a] Department of Industrial Engineering, University of Padova, I-35131, Italy
[b] Department of Materials Science and Engineering, Delft University of Technology, 2628, CD Delft, the Netherlands

ARTICLE INFO

Keywords:
Contact
Rough surfaces
Simulation
Compressibility

ABSTRACT

Contact between elastic bodies with self-affine rough surfaces is mostly studied with a focus on determining surface fields, despite body fields are of great importance to establish, for instance, when and where elasticity breaks down. This work aims at analyzing the effect of contact roughness on the body fields of compressible frictionless solids modeled using Green's function molecular dynamics. Although area-load curves are insensitive to changes in the Hurst exponent as long as they are correctly normalized and are clearly not affected by compressibility, the Von-Mises stress is found to depend on both Hurst exponent and Poisson's ratio.

1. Introduction

Roughness in a self-affine surface spans over multiple length-scales. With the smallest wavelength scaling down to nanometer dimensions, asperities induce significant contact stresses even when subject to moderate loads. This results in severe sub-surface stress concentrations, which can lead to plastic deformation and even to the failure of a tribo-system. In this work we aim at predicting how the Von Mises stress in the body is related to the Hurst exponent of the surface and to the compressibility of the material.

Various methods exist to model the contact response of solids with self-affine surfaces [1–5]. Considering that the numerical description of contact with roughness spanning over various orders of length scales demands fine discretizations, the most efficient numerical methods are the Fast-Fourier-transform based Boundary-Element Methods (FFT-BEM) [6–11]. In these techniques, the contact is modeled in the Fourier domain where the harmonic modes of displacements decouple. This enables their independent energy minimization, which renders the FFT-BEM techniques significantly faster and thereby more suited to study contact-mechanical problems compared to the versatile finite element method [12,13].

Among the FFT-BEM techniques is the Green's function molecular dynamics (GFMD) method, which was successfully used for simulation of the normal contact between rough elastic bodies [7,14,15], and also applied to elasto-plastic [16] and viscoelastic bodies [17]. It was demonstrated in the contact mechanics challenge that the predictions of mean-gap, true contact-area and the proportionality coefficient (κ) of load-area obtained using GFMD agrees quite well with analytical theories and experiments conducted in the linear elastic regime [18]. The technique was recently applied by Müser et al. [19] to estimate the decay of the Von-Mises stress with indentaion depth and thereby provide a very quick estimate of the probability of plastic deformation at different depths from the surface. In this work we will extend the GFMD model to account for the deformation of compressible finite bodies that are free to deform in all three directions. The latter is in our opinion an important extension, because, even in the case of frictionless contact between incompressible bodies, the displacements in the direction normal to the loading in the body are non zero, even if they are zero at the interface. This entails that the corresponding stresses are also non zero and do contribute to the Von Mises stress.

The content of the paper is organized as follows: a brief introduction to the GFMD technique is given in Sec.2; in Sec.3 the Green's function tensor is derived, in Sec.4 the Green's functions and internal stresses are validated by comparing GFMD simulation results for a frictionless Hertzian contact against FEM. In Sec.5 the effect of Hurst exponent, compressibility and Gaussinity on the Von Mises stress are shown and discussed. The notation used in the manuscript is listed in Table 1.

2. Modeling contact with GFMD

The Green's function based boundary integral formulation for an arbitrary contact problem is given as

* Corresponding author. Department of Industrial Engineering, University of Padova, I-35131, Italy.
E-mail address: l.nicola@tudelft.nl (L. Nicola).

https://doi.org/10.1016/j.triboint.2021.106867
Received 23 September 2020; Received in revised form 31 December 2020; Accepted 6 January 2021
Available online 18 January 2021

Table 1
Notation.

Variable	Description
$u_i(\mathbf{r})$	nodal surface displacements
$u_i(\mathbf{q})$	harmonic modes of the surface displacements
$\widetilde{\sigma}_{ij}$	components of the stress tensor
C_{ij}	coefficients of elasticity
E^*	effective Young's modulus
$C(\mathbf{q})$	power spectral density of the self-affine rough indenter
λ_s	smallest wavelength in the roughness Spectrum
q_l	Wave-vector corresponding to the longest wavelength
H	Hurst exponent
$\widetilde{\Delta}_G(q_x, q_y)$	harmonic modes of the Gaussian signal
$h(\mathbf{r})$	roughness height
$\overline{g}_r$	mean-squared gradient of the deformed Contact
σ^{lmax}	local stress maxima in the deformed Substrate
G_{VM}	autocorrelation of the Von-Mises stresses

$$u_i(\mathbf{r}) = \int_S G_{ij}(\mathbf{r}-\mathbf{r}')t_j(\mathbf{r}')d\mathbf{r}', \tag{1}$$

where $G_{ij}(\mathbf{r}-\mathbf{r}')$ is the component of the Green's function tensor which gives the effect of the tractions $t_j(\mathbf{r}')$ imposed at the location $\mathbf{r}'$ on the displacements $u_i(\mathbf{r})$ at the location $\mathbf{r}$ of the boundary layer S. The non-local character of the above boundary equation is eliminated in GFMD by formulating Eq. (1) in the Fourier domain as

$$\widetilde{u}_i(\mathbf{q}) = \widetilde{G}_{ij}(\mathbf{q})\widetilde{t}_j(\mathbf{q}). \tag{2}$$

The Fourier transformed components of the Green's function tensor $\widetilde{G}_{ij}(\mathbf{q})$ relate the displacement modes $\widetilde{u}_i(\mathbf{q})$ to the traction modes $\widetilde{t}_j(\mathbf{q})$ for a given wavevector $\mathbf{q}$.

Once the Green's function tensor is known, a displacement or traction prescribed problem where the contact area is known apriori can be solved in the Fourier domain via simple algebraic operations. However, for cases where the contact area is not known apriori, the equilibrium solution is solved using damped dynamics in Fourier domain [7,16,20].

3. Analytical derivation of the 3-D Green's function tensor

In this section, we derive the Green's function tensor of a three-dimensional isotropic linear elastic layer having a finite height and generic elastic property. To this end, we first obtain the displacement fields in the deformed layer by solving the elastic equilibrium equations coupled with the constitutive relations:

$$\begin{aligned}
&\left[C_{44}\left(\partial_z^2+\partial_y^2\right)+C_{11}\partial_x^2\right]u_x+(C_{12}+C_{44})\partial_x\partial_y u_y+(C_{12}+C_{44})\partial_z\partial_x u_z=0,\\
&\left[C_{44}\left(\partial_x^2+\partial_z^2\right)+C_{11}\partial_y^2\right]u_y+(C_{12}+C_{44})\partial_x\partial_y u_x+(C_{12}+C_{44})\partial_z\partial_y u_z=0,\\
&\left[C_{44}\left(\partial_x^2+\partial_y^2\right)+C_{11}\partial_z^2\right]u_z+(C_{12}+C_{44})\partial_z\partial_y u_y+(C_{12}+C_{44})\partial_z\partial_x u_x=0.
\end{aligned} \tag{3}$$

Here C_{ij} are the coefficients of the elastic tensor and $u = u(x,y,z)$ are the displacements.

Applying 2-D in-plane Fourier transformation to the above set of equations gives the following system of coupled ordinary differential equations (ODE):

$$\begin{aligned}
&s\left[(iq_y)^2\widetilde{u}_x(\mathbf{q},z)+(iq_x)(iq_y)\widetilde{u}_y(\mathbf{q},z)+(iq_x)\frac{\partial\widetilde{u}_z(\mathbf{q},z)}{\partial z}+\frac{\partial^2\widetilde{u}_x(\mathbf{q},z)}{\partial z^2}\right]+(1-2s)\left[(iq_x)(iq_y)\widetilde{u}_y(\mathbf{q},z)+(iq_x)\frac{\partial\widetilde{u}_z(\mathbf{q},z)}{\partial z}\right]+(iq_x)^2\widetilde{u}_x(\mathbf{q},z)=0,\\
&s\left[(iq_x)^2\widetilde{u}_y(\mathbf{q},z)+(iq_y)(iq_x)\widetilde{u}_x(\mathbf{q},z)+(iq_y)\frac{\partial\widetilde{u}_z(\mathbf{q},z)}{\partial z}+\frac{\partial^2\widetilde{u}_y(\mathbf{q},z)}{\partial z^2}\right]+(1-2s)\left[(iq_x)(iq_y)\widetilde{u}_x(\mathbf{q},z)+(iq_y)\frac{\partial\widetilde{u}_z(\mathbf{q},z)}{\partial z}\right]+(iq_y)^2\widetilde{u}_y(\mathbf{q},z)=0,\\
&s\left[(iq_x)^2\widetilde{u}_z(\mathbf{q},z)+(iq_y)^2\widetilde{u}_z(\mathbf{q},z)+(iq_x)\frac{\partial\widetilde{u}_x(\mathbf{q},z)}{\partial z}+(iq_y)\frac{\partial\widetilde{u}_y(\mathbf{q},z)}{\partial z}\right]+\frac{\partial^2\widetilde{u}_z(\mathbf{q},z)}{\partial z^2}+(1-2s)\left[(iq_x)\frac{\partial\widetilde{u}_x(\mathbf{q},z)}{\partial z}+(iq_y)\frac{\partial\widetilde{u}_y(\mathbf{q},z)}{\partial z}\right]=0.
\end{aligned} \tag{4}$$

Here $s=\frac{C_{44}}{C_{11}}$ and $\widetilde{u}_x(\mathbf{q},z)$, $\widetilde{u}_y(\mathbf{q},z)$, $\widetilde{u}_z(\mathbf{q},z)$ are the in-plane displacements. Finally, the above set of ODEs are reduced to the following set of linear algebraic equations:

$$\begin{bmatrix}\widetilde{u}_x(\mathbf{q},z)\\ \widetilde{u}_y(\mathbf{q},z)\\ \widetilde{u}_z(\mathbf{q},z)\end{bmatrix}=\left[f_{ij}(\mathbf{q},z)\right]\begin{bmatrix}a_1(\mathbf{q})\\ a_2(\mathbf{q})\\ a_3(\mathbf{q})\\ a_4(\mathbf{q})\\ a_5(\mathbf{q})\\ a_6(\mathbf{q})\end{bmatrix}. \tag{5}$$

The elements of the matrix $[f_{ij}(\mathbf{q},z)]$ are:

$$
\begin{aligned}
f_{11}(\mathbf{q},z) &= \frac{2sq_{\mathrm{r}}\cosh(zq_{\mathrm{r}}) - (s-1)zq_x^2\sinh(zq_{\mathrm{r}})}{(s+1)q_{\mathrm{r}}},\\
f_{12}(\mathbf{q},z) &= \frac{2q_x^2((s+1)\sinh(zq_{\mathrm{r}}) - (s-1)zq_{\mathrm{r}}\cosh(zq_{\mathrm{r}}))}{2(s+1)q_{\mathrm{r}}^3} + \frac{4q_y^2\sinh(zq_{\mathrm{r}})}{2(s+1)q_{\mathrm{r}}^3},\\
f_{13}(\mathbf{q},z) &= f_{21}(\mathbf{q},z) = -\frac{(s-1)zq_xq_y\sinh(zq_{\mathrm{r}})}{(s+1)q_{\mathrm{r}}},\\
f_{14}(\mathbf{q},z) &= f_{22}(\mathbf{q},z) = \frac{(s-1)q_xq_y(\sinh(zq_{\mathrm{r}}) - zq_{\mathrm{r}}\cosh(zq_{\mathrm{r}}))}{(s+1)q_{\mathrm{r}}^3},\\
f_{15}(\mathbf{q},z) &= f_{31}(\mathbf{q},z) = \frac{i(s-1)q_x(zq_{\mathrm{r}}\cosh(zq_{\mathrm{r}}) - \sinh(zq_{\mathrm{r}}))}{(s+1)q_{\mathrm{r}}},\\
f_{16}(\mathbf{q},z) &= f_{32}(\mathbf{q},z) = \frac{i(s-1)zq_x\sinh(zq_{\mathrm{r}})}{(s+1)q_{\mathrm{r}}},\\
f_{23}(\mathbf{q},z) &= \frac{2sq_{\mathrm{r}}\cosh(zq_{\mathrm{r}}) - (s-1)zq_y^2\sinh(zq_{\mathrm{r}})}{(s+1)q_{\mathrm{r}}},\\
f_{24}(\mathbf{q},z) &= \frac{q_y^2((s+1)\sinh(zq_{\mathrm{r}}) - (s-1)zq_{\mathrm{r}}\cosh(zq_{\mathrm{r}}))}{(s+1)q_{\mathrm{r}}^3} + \frac{2q_x^2\sinh(zq_{\mathrm{r}})}{(s+1)q_{\mathrm{r}}^3},\\
f_{25}(\mathbf{q},z) &= f_{33}(\mathbf{q},z) = \frac{i(s-1)q_y(zq_{\mathrm{r}}\cosh(zq_{\mathrm{r}}) - \sinh(zq_{\mathrm{r}}))}{(s+1)q_{\mathrm{r}}},\\
f_{34}(\mathbf{q},z) &= \frac{i(s-1)zq_y\sinh(zq_{\mathrm{r}})}{(s+1)q_{\mathrm{r}}},\\
f_{35}(\mathbf{q},z) &= \frac{(s-1)zq_{\mathrm{r}}^2\sinh(zq_{\mathrm{r}}) + 2q_{\mathrm{r}}\cosh(zq_{\mathrm{r}})}{(s+1)q_{\mathrm{r}}},\\
f_{36}(\mathbf{q},z) &= \frac{(s-1)z\cosh(zq_{\mathrm{r}})}{s+1} + \frac{\sinh(zq_{\mathrm{r}})}{q_{\mathrm{r}}},
\end{aligned}
\tag{6}
$$

where $q_{\mathrm{r}} = \sqrt{q_x^2+q_y^2}$.

The six unknowns $a_i(\mathbf{q})$ in Eq. (5) are determined from the boundary conditions at the top and the bottom surfaces of the elastic layer. In the case of displacement prescribed boundary value problems these unknowns are directly evaluated from Eq. (5). In the case of traction prescribed boundary value problems the unknowns are evaluated through the following stress-strain relations

$$
\begin{bmatrix}\widetilde{\sigma}_{zz}(\mathbf{q},z)\\ \widetilde{\sigma}_{yz}(\mathbf{q},z)\\ \widetilde{\sigma}_{zx}(\mathbf{q},z)\end{bmatrix} = [C_{ij}]\begin{bmatrix}(iq_x)\widetilde{u}_x(\mathbf{q},z)\\ (iq_y)\widetilde{u}_y(\mathbf{q},z)\\ \dfrac{\partial u_z(\mathbf{q},z)}{\partial z}\\ \dfrac{\partial u_x(\mathbf{q},z)}{\partial z} + (iq_x)\widetilde{u}_z(\mathbf{q},z)\\ \dfrac{\partial u_y(\mathbf{q},z)}{\partial z} + (iq_y)\widetilde{u}_z(\mathbf{q},z)\end{bmatrix},
$$

$$
C_{ij} = \begin{bmatrix}C_{12} & C_{12} & C_{11} & 0 & 0\\ 0 & 0 & 0 & C_{44} & 0\\ 0 & 0 & 0 & 0 & C_{44}\end{bmatrix},
\tag{7}
$$

by substituting the stress values with tractions at the boundaries z_0 and z_m. After the unknowns $a_i(\mathbf{q})$ are evaluated, they are substituted back into Eq. (5). This gives the relation between the surface displacements and tractions as

$$
\begin{bmatrix}\widetilde{u}_x(\mathbf{q},z_{\mathrm{m}})\\ \widetilde{u}_y(\mathbf{q},z_{\mathrm{m}})\\ \widetilde{u}_z(\mathbf{q},z_{\mathrm{m}})\\ \widetilde{u}_x(\mathbf{q},z_0)\\ \widetilde{u}_y(\mathbf{q},z_0)\\ \widetilde{u}_z(\mathbf{q},z_0)\end{bmatrix} = \left[\widetilde{G}_{ij}(\mathbf{q})\right]\begin{bmatrix}\widetilde{t}_x(\mathbf{q},z_{\mathrm{m}})\\ \widetilde{t}_y(\mathbf{q},z_{\mathrm{m}})\\ \widetilde{t}_z(\mathbf{q},z_{\mathrm{m}})\\ \widetilde{t}_x(\mathbf{q},z_0)\\ \widetilde{t}_y(\mathbf{q},z_0)\\ \widetilde{t}_z(\mathbf{q},z_0)\end{bmatrix},
\tag{8}
$$

where the elements of the Green's function tensor $[\widetilde{G}_{ij}(\mathbf{q})]$, assuming $z_0 = 0$, are given in A.

The reader can see that in the limiting case of a frictionless semi-infinite elastic half-space, the displacements at the surface reduce to those given by the Boussinesq solution [21],

$$
u_i(\mathbf{q},z_{\mathrm{m}}) = \widetilde{G}_{iz}(\mathbf{q},z_{\mathrm{m}})t_z(\mathbf{q},z_{\mathrm{m}}),
\tag{9}
$$

where

$$
\begin{aligned}
\widetilde{G}_{xz}(\mathbf{q},z_{\mathrm{m}}) &= \frac{i(\nu+1)(2\nu-1)q_x}{E\left(q_x^2+q_y^2\right)},\\
\widetilde{G}_{yz}(\mathbf{q},z_{\mathrm{m}}) &= \frac{i(\nu+1)(2\nu-1)q_y}{E\left(q_x^2+q_y^2\right)},\\
\widetilde{G}_{zz}(\mathbf{q},z_{\mathrm{m}}) &= -\frac{2(\nu^2-1)}{E\sqrt{q_x^2+q_y^2}},
\end{aligned}
\tag{10}
$$

while the other Green's tensor components $\widetilde{G}_{zz}(\mathbf{q},z_0), \widetilde{G}_{xz}(\mathbf{q},z_0)$ and $\widetilde{G}_{yz}(\mathbf{q},z_0)$ tend to zero as the distance between the top and the bottom surfaces becomes infinite.

4. Validation of the model: Hertzian indentation

4.1. Surface fields compared with analytical solution

Firstly, we consider the frictionless indentation of a rigid sphere on an elastic half-space and compare the results of the simulation with Hertz theory [22] (refer Fig. 1). The analytical Hertzian solution is first derived for a two-dimensional array of indenters that are equally spaced in the $x-$ and $y-$ directions. This is done to enable a comparison with the GFMD solution which is intrinsically periodic. The normal surface displacement $u_z(r_i)$ reads

$$
\begin{aligned}
u_z(r_i) &= \frac{1-\nu^2}{E}\frac{3P_{\mathrm{o}}}{8a_r}\left[\pi\left(2a_r^2-r_i^2\right) + 2u_z^{\mathrm{pt}}\right], \forall r_i \le a_r\\
u_z(r_i) &= \frac{1-\nu^2}{E}\frac{3P_{\mathrm{o}}}{4a_r}\left[\left(2a_r^2-r_i^2\right)\sin^{-1}\frac{a_r}{r_i} + a_r r_i\left(1-\frac{a_r^2}{r_i^2}\right)^{0.5} + u_z^{\mathrm{pt}}\right], \forall r_i \ge a_r
\end{aligned}
\tag{11}
$$

Here,

$$
u_z^{\mathrm{pt}} = \sum_{\substack{k=-\infty\\ k\neq 0}}^{\infty}\sum_{\substack{l=-\infty\\ l\neq 0}}^{\infty}\left[\left(2a_r^2-r_{\mathrm{d}}^2\right)\sin^{-1}\frac{a_r}{r_{\mathrm{d}}} + a_r r_{\mathrm{d}}\left(1-\frac{a_r^2}{r_{\mathrm{d}}^2}\right)^{0.5}\right].
\tag{12}
$$

$$
r_{\mathrm{d}} = \sqrt{\left(L_x k - x_i\right)^2 + \left(L_y l - y_i\right)^2},
\tag{13}
$$

r_i is the location at which the displacement is evaluated, a_r is the contact radius and P_{o} is the mean pressure. The terms included in the summation represent the contribution to the displacement from periodic replicas centered at $(L_x k, L_y l)$, where k and l take integer values.

Also note that, using simple geometry, the normal displacement

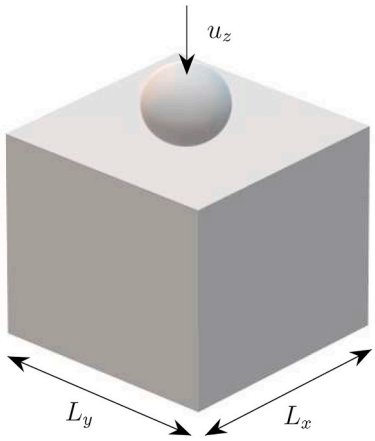

Fig. 1. Schematic representation of a unit cell of elastic substrate indented by a Hertzian punch.

within the region of a spherical contact is evaluated from the radius of curvature R and the indentation depth u_z^o as

$$u_z(r_i) = u_z^o - \frac{r_i^2}{2R}, \forall r_i \leq a_r \tag{14}$$

Using the above Eqs. 11–14, the mean pressure is expressed in terms of the contact radius and indenter curvature as

$$P_o = \frac{1}{\left(u_z^{t1} - u_z^{t2}\right)} \frac{4Ea_r^3}{3R(1-\nu^2)} \tag{15}$$

where,

$$u_z^{t1} = \pi\left(2a_r^2\right) + 2\sum_{k=-\infty}^{\infty}\sum_{l=-\infty}^{\infty}\left[\left(2a_r^2 - r_d(0)^2\right)\sin^{-1}\frac{a_r}{r_d(0)} + a_r r_d\left(0\right)\left(1-\frac{a_r^2}{r_d(0)^2}\right)^{0.5}\right],$$

$$k\neq 0 \quad l\neq 0$$

$$u_z^{t2} = \pi\left(a_r^2\right) + 2\sum_{k=-\infty}^{\infty}\sum_{l=-\infty}^{\infty}\left[\left(2a_r^2 - r_d(a_r)^2\right)\sin^{-1}\frac{a_r}{r_d(a_r)} + a_r r_d\left(a_r\right)\left(1-\frac{a_r^2}{r_d(a_r)^2}\right)^{0.5}\right],$$

$$k\neq 0 \quad l\neq 0$$

$$r_d\left(0\right) = \sqrt{(L_x k)^2 + (L_y l)^2},$$

$$r_d\left(a_r\right) = \sqrt{(L_x k - a_r)^2 + (L_y l)^2}. \tag{16}$$

The mean pressure evaluated using Eq. (15) for a given contact radius and indenter curvature is imposed onto the surface layer in the GFMD simulation. The GFMD layer with a unit aspect ratio is discretized with $nx \times ny$ discretization points, where nx, ny are equal to 128. The Young's modulus of the substrate was chosen to be 70 GPa. Three different values of the Poisson's ratio are considered to see the effect of compressibility on the material response.

The equilibrium solution in GFMD is obtained through damped dynamic energy minimization. Herein, the motion of the modal displacements towards equilibrium is integrated using the position-Störmer-Verlet scheme. The harmonic modes are slightly under-damped with a damping factor that is $0.99\eta_{cr}$, where η_{cr} is the critical damping factor of the slowest mode. This ensures convergence of the displacements to their correct equilibrium position. The critical damping factor of the principal mode for a semi-infinite halfspace was derived in the work of Prodanov *et al.* [7] as,

$$\eta_{cr} \propto \left(\frac{P_0}{E^* \bar{g}}\right)^{\alpha} \sqrt{\frac{\beta}{L_x}}, \tag{17}$$

Here, E^* is the effective modulus, $\bar{g}$ is the root mean squared gradient of the surface profile. α and β are positive real valued parameters that depend on L_x and are found empirically. We use the hard-wall interactions at the interface to avoid inter-penetration between the substrate and the Hertzian punch.

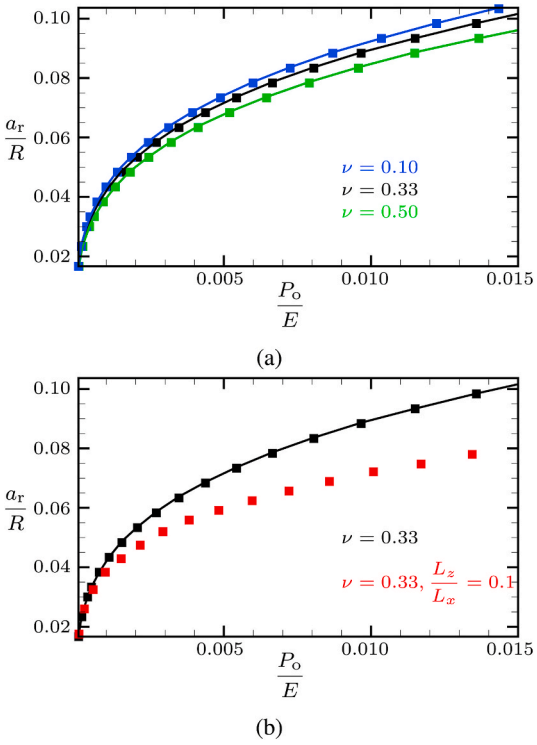

Fig. 2. GFMD (squared symbols) and Hertz theory (solid line) solutions: (a) The effect Poisson's ratio on the load-area curves, (b) The effect of substrate thickness on the load-area curves.

In Fig. 2, the solid lines represent the analytical solution and the solid squares the GFMD solution. Fig. 2a shows the effect of Poisson's ratio on the load-area curves. As expected, stiffness increases with Poisson's ratio. While the analytical solution describes the behavior of an infinite body only, the simulations can now model also a slab of material. The elastic slab is modeled as a periodic cubic unit cell ($L_x = L_y = L_z$) and is indented to a depth u_z^0 such that $u_z^0/L_x = 0.02L_z/R$. The Young's modulus and Poisson's ratio of the elastic slab are chosen to be 70 GPa and 0.33, respectively. Fig. 2b confirms that a slab is stiffer than the infinte solid.

4.2. Validation of the GFMD body fields through comparison with FEM

The body fields derived in Sec. 3 are validated through a quick comparison with the results obtained from a finite element analysis of the Hertzian indentation of a finite slab, to gain confidence in our method and then proceed with addressing rough contacts. The FEM simulations are performed using the commercial software Abaqus. A mesh sensitivity analysis lead us to discretize the 3-D unit cell into 64 × 64 × 64 brick elements. These elements are fully integrated 20-node type in the bulk region. The near-surface region of the cubic unit cell

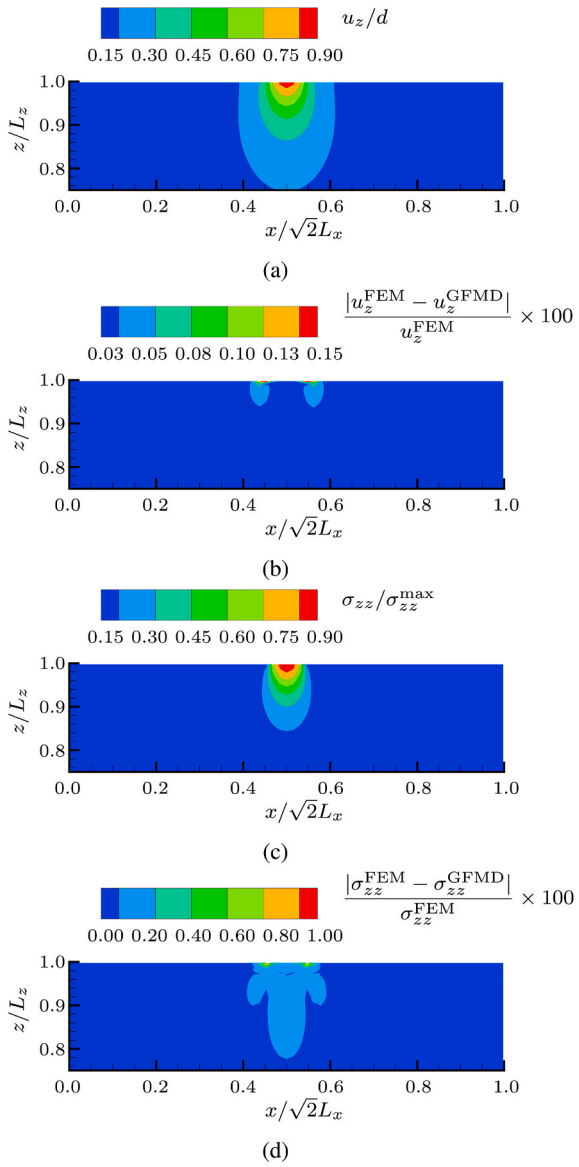

Fig. 3. The normal component of displacement (a) and stress fields (c) are shown under a Hertzian contact along with the corresponding relative differences between the GFMD and FEM solutions.

is discretized into fully integrated 27-node brick elements. In the case of GFMD, a discretization 32 × 32 did suffice, but we used anyhow 64× 64 for the sake of comparison.

In GFMD, equilibration is obtained by damping the harmonic modes with the critical damping factor of the slowest mode:

$$\eta_{\mathrm{cr}} = \frac{2}{\Delta t}\sqrt{\frac{E}{2L_z(1+\nu)}} - \frac{E}{2L_z(1+\nu)}, \tag{18}$$

where Δt is the time step. In the FEM analysis, the total indentation is applied in several adaptive incremental steps. For each of the tentative incremental steps, equilibrium is assumed to be reached when the force residual at all the nodes is less than 0.5% of the average nodal forces in the solid. If the solution has not converged within 16 iterations or if the solution appears to diverge, the tentative increment is reduced by a factor 0.25. If, instead, less than five iteration are required to reach convergence for two increments in a row the subsequent incremental step is increased by a factor 0.5.

Fig. 3a and c present the normal displacement and normal stress

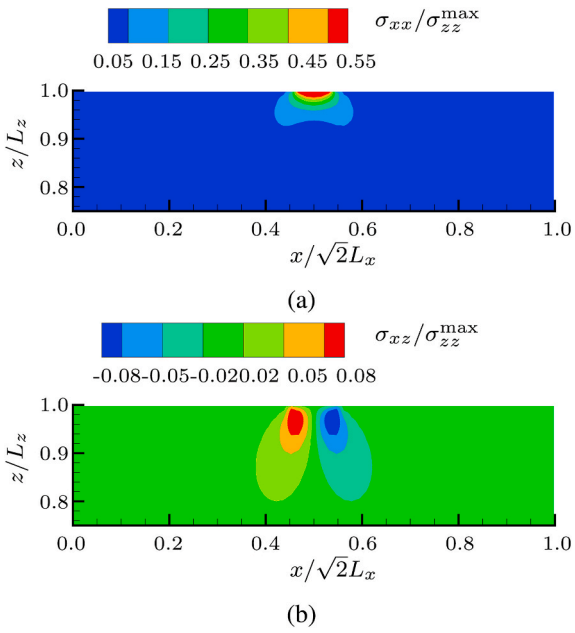

Fig. 4. Tensile (σ_{xx}) and shear (σ_{xz}) stress components under a Hertzian contact.

fields along the diagonal plane of the substrate, as obtained from GFMD. In Fig. 3b and d, the relative differences are shown between the solutions obtained through GFMD and FEM. It is seen from the figures that the results obtained using GFMD differ from those obtained using FEM 1.0%. As expected, their differences are concentrated mostly near the edges of the contact region. The tensile and shear stresses under a Hertzian contact are shown along the diagonal plane in Fig. 4a and Fig. 4b, respectively. The relative errors for both tensile and shear stresses are also below 1.0%, but not shown here.

5. Indentation with a rough rigid surface

5.1. Description of surface roughness

The rough surfaces are generated using the Power Spectral Density (PSD) method, which gives the PSD of a self-affine surface as the power-law relation

$$\mathrm{C}(\mathbf{q}) = \mathrm{C}_0 \left(\frac{q_1}{\mathbf{q}}\right)^{2H+2}. \tag{19}$$

Here H is the Hurst exponent and q_1 is the wavevector corresponding to the longest wavelength contained in the surface. C_0 is a real valued constant that is varied to obtain a rough surface with a given root-mean-square (rms) height. A roughness profile $\widetilde{h}(q_x, q_y)$ is created by the convolution of the PSD with a Gaussian signal,

$$\widetilde{h}(q_x, q_y) = \widetilde{\Delta}_{\mathrm{G}}(q_x, q_y)\sqrt{\mathrm{C}(\mathbf{q})}. \tag{20}$$

Here a Gaussian complex variable $\widetilde{\Delta}_{\mathrm{G}}(q_x, q_y)$ is obtained by the Box-Muller transform [23],

$$\begin{aligned} \mathscr{R}\left\{\widetilde{\Delta}_{\mathrm{G}}\right\}(q_x, q_y) &= \sqrt{-2\ln(U_1)}\cos(2\pi U_2), \\ \mathscr{I}\left\{\widetilde{\Delta}_{\mathrm{G}}\right\}(q_x, q_y) &= \sqrt{-2\ln(U_1)}\sin(2\pi U_2), \end{aligned} \tag{21}$$

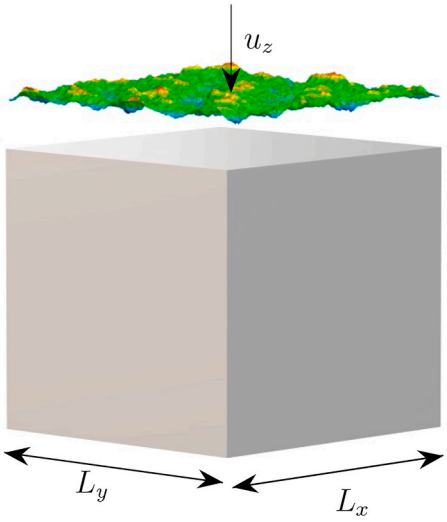

Fig. 5. Schematic representation of the indentation of the unit cell of an elastic flat substrate by a rigid rough indenter. Different colors in the rough indenter represent different heights of the self-affine rough surface. (For interpretation of the references to color in this figure legend, the reader is referred to the Web version of this article.)

with U_1 and U_2 being the independent random numbers that are uniformly distributed between the interval $[0, 1]$. The sinusoids in Eq. (21) are given a random phase and this ensures that the generated height distributions best mimic the experimentally observed surface roughness as a random process [24]. Additionally, since real surfaces are self-affine only in a certain range of length-scales, the in-plane wave-vectors q_x, q_y that constitute a roughness profile are made to span over a maximum of three orders of magnitude between q_s and q_l. Where q_s and q_l are the wavevectors of the longest (λ_l) and shortest wavelength (λ_s) of the surface, respectively.

5.2. Effect of Hurst exponent

An isotropic linear elastic flat solid represented by a periodic unit cell with a unit aspect ratio is deformed by indenting with a rough indenter with RMS height $L_x/1000$ to a contact area fraction of $a_r = 10\%$ (see Fig. 5). Two different values are considered for the Hurst exponent of the indenter, i.e. H = 0.2 and 0.8 (refer Fig. 6).

The shortest and longest wavelength are $\lambda_s = L_x/256$ and $\lambda_l = L_x/8$. At the beginning of the simulation, the indenter is positioned such that the bottom-most point is in contact with the substrate and it does not exert any pressure. This means that the average spacing between surfaces is larger when the RMS height is larger.

The surface is discretized with 2048 × 2048 nodes. Following Müser et al. [7], the discretization of the surface is selected to be $\lambda_s/8 \times \lambda_s/8$ in both the directions. The Von Mises stress fields are evaluated analytically on an equispaced 3D grid with grid points also spaced by $\lambda_s/8$ in order to capture the sub-surface stress peaks corresponding to the smallest wavelengths. The local stress maxima that occur underneath each contact area ($\sigma_{\mathrm{VM}}^{\mathrm{lmax}}$) are identified by picking the Von Mises stress values that exceed the values at the neighboring nodes. To evaluate the peak stress statistics, the probability density function of the local maxima is calculated, by grouping the N values of $\sigma_{\mathrm{VM}}^{\mathrm{lmax}}$ into 100 bins of width w_{bin}. The same procedure is used to calculate the probability density funcion of the traction peaks t_3^{lmax}, to see if there is a one-to one correlation between surface and Von-Mises peaks.

The traction distributions obtained at a contact fraction of 10% in Fig. 7 show that, as expected, a smaller Hurst exponent gives rise to finer

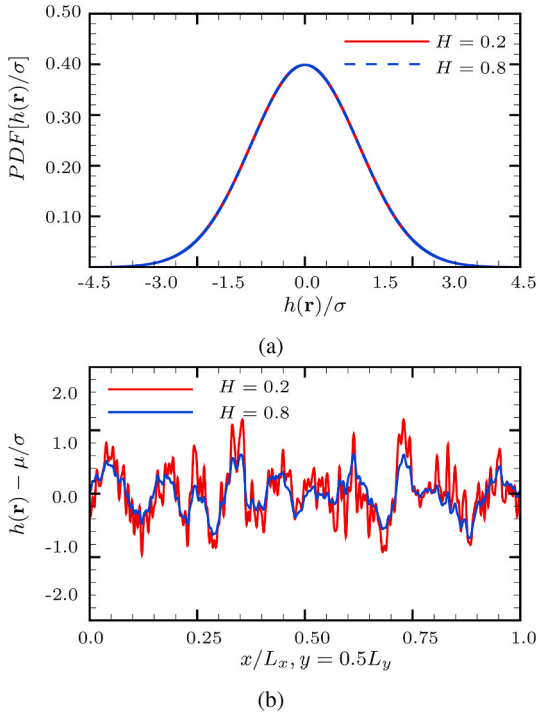

Fig. 6. (a) Probability density function of the surface heights and (b) cross-section of the surface for $H = 0.2$ and $H = 0.8$.

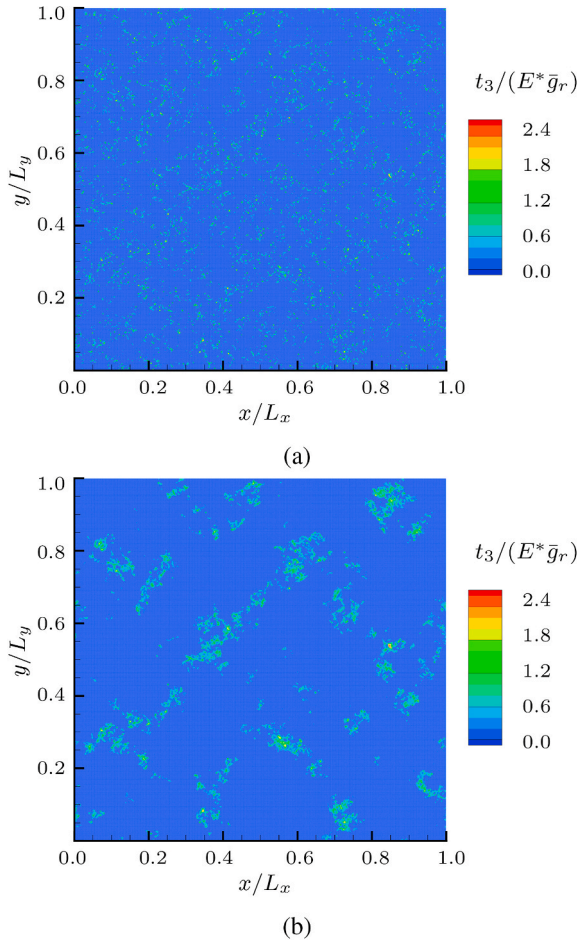

Fig. 7. Traction distribution ($t_3/E^*\bar{g}_r$) for a) H = 0.2, b) H = 0.8.

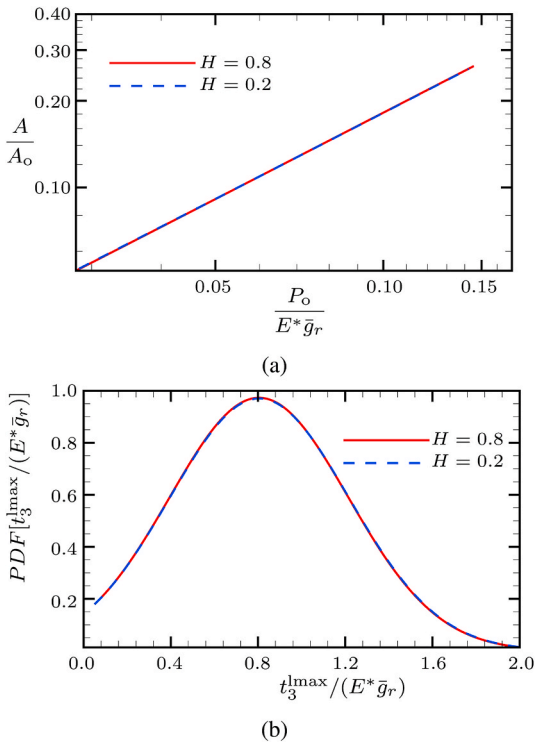

Fig. 8. (a) Relative contact-area a_r versus normalized nominal-pressure $P_0/(E^*\bar{g}_r)$ for different Hurst exponents. (b) Probability density function of the traction peaks PDF$[t_3/E^*\bar{g}_r]$.

and more dispersed local contacts.

It is well-known that there is a linear relation between relative true contact area a_r and normalized load $P_o/(E^*\bar{g}_r)$, where $\bar{g}_r$ is the root mean square gradient of the true contact. With this normalization, the curves

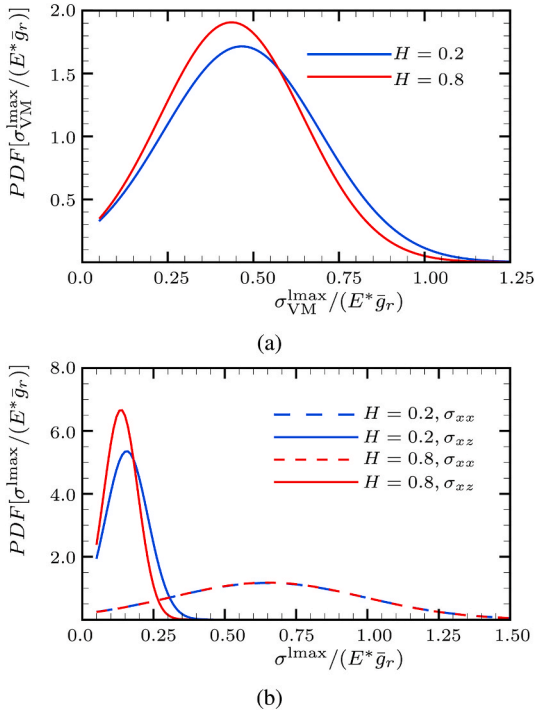

Fig. 9. Effect of Hurst exponent on the probability density function of a) the Von Mises stress peaks, σ_{VM}^{lmax} and b) on the peaks of σ_{xx} i.e. σ_{xx}^{lmax}, and of σ_{xz} i.e. σ_{xz}^{lmax}, for bodies with $\nu = 0.33$.

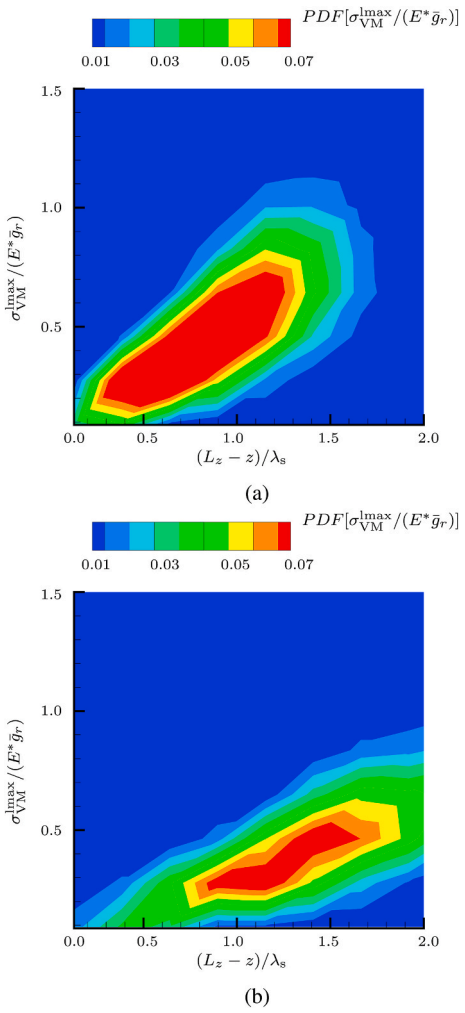

Fig. 10. Distributions of $\sigma_{VM}/E^*\bar{g}_r$ along the depth of the body for (a) H = 0.2 and (b) H = 0.8. The Poisson's ratio is $\nu = 0.33$.

for different Hurst exponents overlap as shown in Fig. 8a. Therefore, also the curves that represent the probability density function of the traction peaks in Fig. 8b overlap.

Nonetheless, the Von Mises stress peaks that are induced underneath the traction peaks at a depth in the body dictated by the size of the local contact area, present a probability density distribution that depends, although not strongly, on the Hurst exponent (see Fig. 9a). The smaller Hurst exponent corresponds to a larger probability of having high stress peaks. This suggests that the stress components contributing to the Von Mises stress, do not all scale as the normal stress component.

To confirm this, we present in Fig. 9b the probability density functions of σ_{xx} and σ_{xz}. The distribution of the tensile stress peaks σ_{xx}^{lmax} is independent of the Hurst exponent, given that σ_{xx} scales as σ_{zz} with the rms gradient. However, this does not hold true for the shear stresses: a smaller value of the Hurst exponent corresponds to larger shear stress peaks σ_{xz}^{lmax}.

In Fig. 10 the distribution of the stress peaks along the depth of the substrate is contrasted for Hurst exponents $H = 0.2$ and 0.8. Consistently with the previous figure, the larger Hurst exponent, leads to a broader distribution of the Von-Mises stress peaks values. One can also see that for the larger Hurst exponent the higher stress peaks are further away from the surface, which is to be expected, given that the depth of the subsurface stress peaks is controlled by the size of the contact patches that induces them, which are larger for $H = 0.8$.

The average decay of the Von-Mises stress peaks into the depth of the

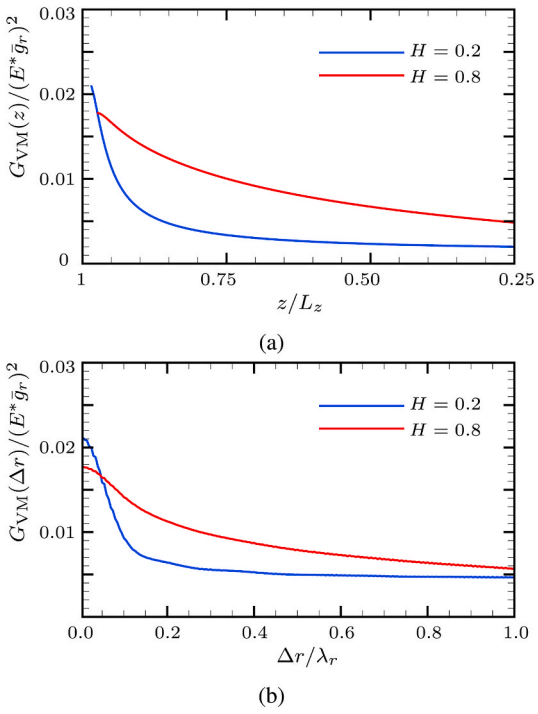

Fig. 11. Effect of the Hurst exponent on the average decay of the sub-surface Von-Mises stress peaks (a) along the depth and (b) along the plane of maximum Von-Mises stress in the substrate.

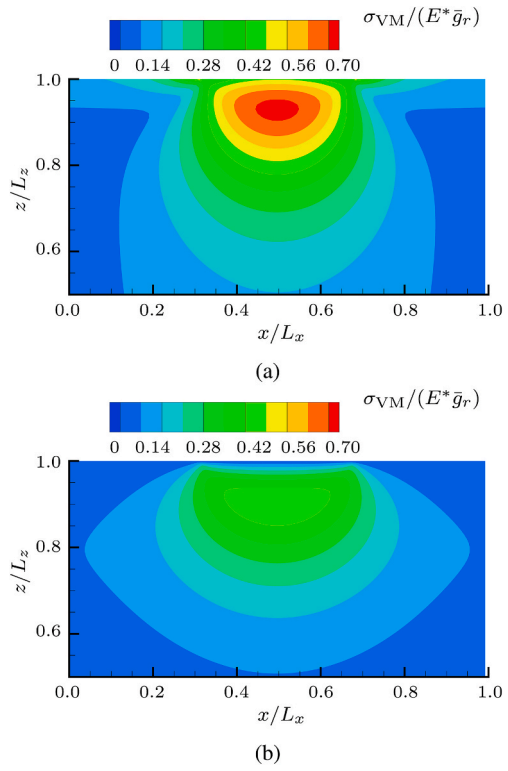

Fig. 12. Von-Mises stress $\sigma_{VM}/(E^*\bar{g}_r)$ for the indentaion with a Hertzian a) $\nu = 0.0$, b) $\nu = 0.5$.

substrate, shown in Fig. 11a can be evaluated by computing the auto-correlation $G_{VM}(z)$.

$$G_{VM}(z) = \left\langle \sigma_{VM}\left(\mathbf{r}, z^{lmax}_{peak}\right)\sigma_{VM}(\mathbf{r}, z)\right\rangle_{\mathbf{r}} - \left\langle \sigma_{VM}\left(\mathbf{r}, z^{lmax}_{peak}\right)\right\rangle_{\mathbf{r}}\left\langle \sigma_{VM}(\mathbf{r}, z)\right\rangle_{\mathbf{r}}, \quad (22)$$

where z^{lmax}_{peak} is the height in the substrate where the largest stress peak is induced. Again, it is the size of the contact patches that control the decay, so the rough contact with smaller Hurst exponent has a faster decay of the stresses.

Similarly, a faster decay is observed in Fig. 11b for the in-plane decay of the stresses. The decay is presented in the plane containing the stress peak with largest magnitude. From Fig. 11, we learn that although rough contacts with small Hurst exponents reach locally larger Von Mises stress, the regions that are subjected to those stresses are very small, given that the stresses decay fast both along the depth and the plane. If plastic deformation were to occur in the subsurface it would be very confined. On the contrary, when the Hurst exponent is large the regions that are affected by a high Von Mises stress are broader. In bodies that show size dependence in the onset of plasticity, as metals, this also means that it is more likely to observe early plasticity in bodies with larger H than with smaller H. In metals this is because the carriers of plastic deformation are dislocations, which nucleate from discrete sources. The probability of finding a dislocation source in a highly stressed region increases with the size of the region itself.

5.3. Effect of compressibility

Although surface tractions in frictionless contacts are insensitive to changes in the Poisson's ratio of the slab, its compressibility is likely to play a role on the subsurface stress components different from σ_{zz}, and consequently on the Von Mises stress. The effect of compressibility on the Von Mises stress obtained by indenting an elastic body with a Hertzian punch is shown in Fig. 12.

For indentation with a rough surface with Hurst exponent 0.8, Fig. 13a shows that the smaller the Poisson's ratio, the broader is the distribution of the Von Mises stress peaks. Additionally, the Von-Mises

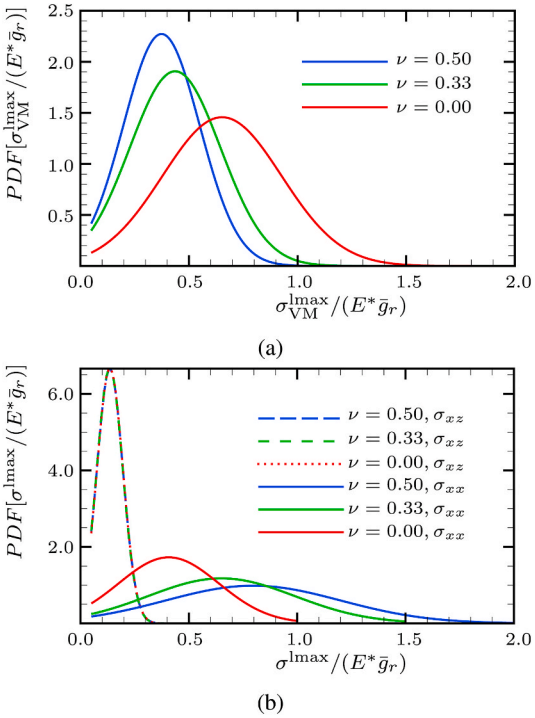

Fig. 13. Effect of Poisson's ratio on the probability density function of a) σ^{lmax}_{VM} b) σ^{lmax}_{xx} and σ^{lmax}_{xz}.

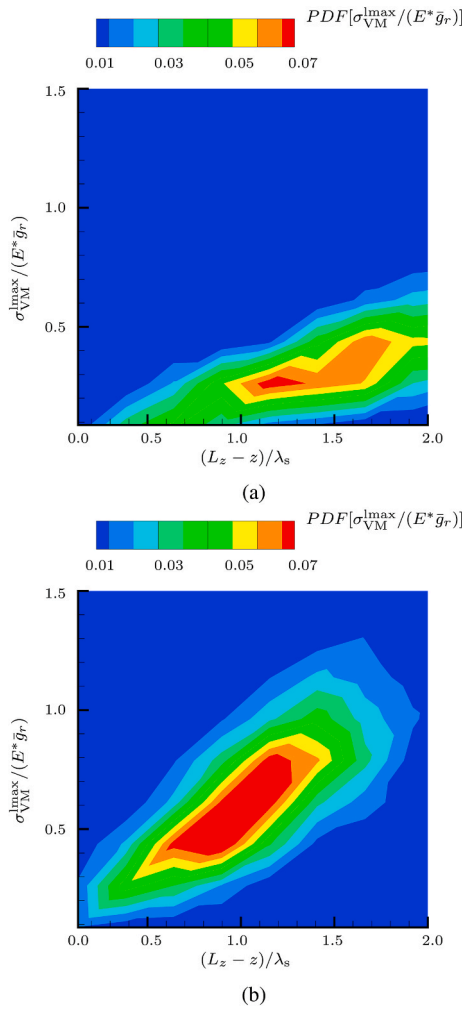

Fig. 14. Effect of Poisson's ratio on the depth dependent distributions of $\sigma_{VM}/E^*\bar{g}_r$: (a) $\nu = 0.5$, (b) $\nu = 0.0$.

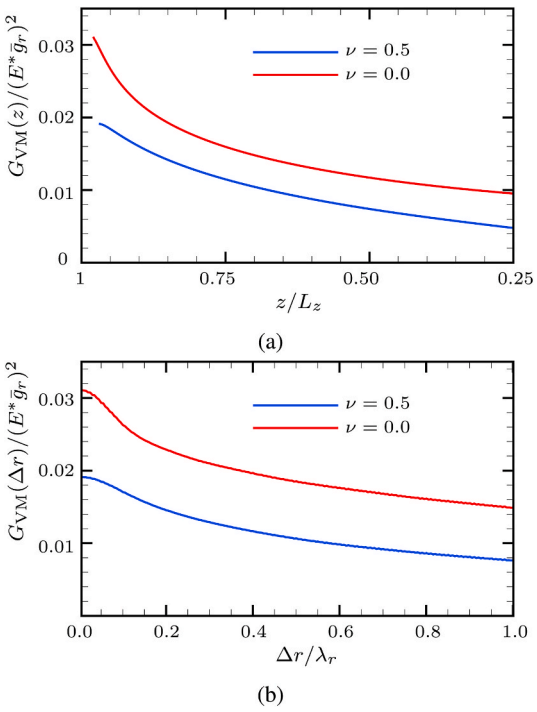

Fig. 15. Effect of Poisson's ratio on the average decay of the sub-surface Von-Mises stress peaks (a) along the depth and (b) along the plane of maximum Von-Mises stress in the substrate.

stress peaks in the subsurface of a fully compressible body reach values that are approximately 1.5 times larger than those in an incompressible body. Thus, the latter is much less likely to deform plastically. Here, it is the shear stress component that does not scale, contrary to the normal stress component, with the rms gradient of the surface (see Fig. 13b).

In Fig. 14, the distribution of stress peaks along the depth of the substrate is shown for Poisson's ratios $\nu = 0$ and 0.5 and Hurst exponent $H = 0.8$. In substrates with smaller Poisson's ratios the Von-Mises stress peaks have a broader distribution, reach larger values, and occur closer to the surface compared to less compressible substrates.

The stress peaks autocorrelation in the depth of the body and in the plane of maximum Von Mises stress in Fig. 15 show negligible differences in the decay of the stresses with compressibility. Thus, a body with smaller Poisson's ratio has not only larger subsurface stress peaks but also larger regions with high Von Mises stress.

5.4. *Effect of skewness and kurtosis of the height distribution*

The surfaces so far considered have a Gaussian distribution of heights. However, it is well known, that most of the common manufacturing processes produce surfaces that have a non-Gaussian distribution height distribution [25]. For example, turning [26] and electro-discharge machining processes [27] produce surfaces that have a positive skewness and low kurtosis. Differently, machining processes such as milling [28–30], grinding [25] produce surfaces that have a negative skewness and high kurtosis. Here, we study the effect of skewness and kurtosis on the internal stresses induced during the indentation to a contact area fraction of 10%. For this, we take the Gaussian rough surface with $H = 0.8$ and $\lambda_s = L_x/128$ that we considered in the previous section and change its skewness and kurtosis independently. The skewness of the surface is changed by applying Johnson's transformation [31] to the Gaussian surface $G(\mathbf{r})$, so that the skewed surface $S(\mathbf{r})$ is defined as:

$$S(\mathbf{r}) = \frac{\lambda e^{V(\mathbf{r})} + \zeta\left(e^{V(\mathbf{r})} + 1\right)}{e^{V(\mathbf{r})} + 1}$$
$$V(\mathbf{r}) = \frac{G(\mathbf{r}) - \gamma}{\delta} \tag{23}$$

The height distributions of the skewed surface $S(\mathbf{r})$ lie within the interval $[\zeta, \zeta + \lambda]$. Here, we take $\zeta = -4$, and $\lambda = 8$. γ and δ are the shape parameters of the skewed surface. The magnitude of the skewness is controlled by δ, which can take only positive real values, its sign by γ. As mentioned before, since both positively skewed and negatively skewed surfaces are commonly encountered in practice, we consider both cases: the positively skewed distribution $S_P(\mathbf{r})$ is generated with $\gamma = 1.25$, the negatively skewed $S_N(\mathbf{r})$ with $\gamma = -1.25$. The surface height

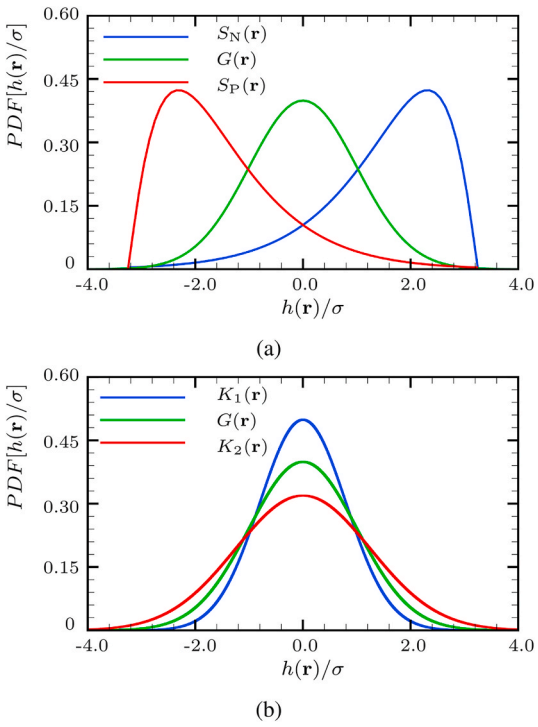

Fig. 16. The height distribution of the rough indenters are shown for different (a) skewness and (b) kurtosis.

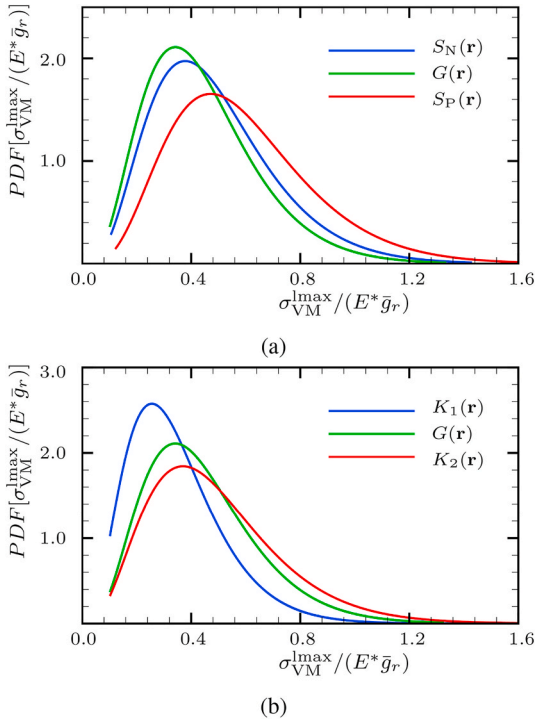

Fig. 17. The effect of (a) skewness and (b) kurtosis of a rough surface on the probability density function of the Von Mises stress peaks.

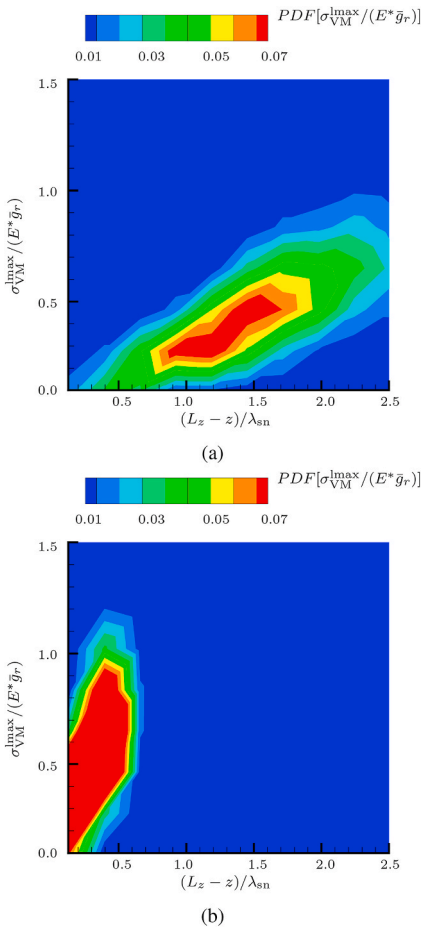

Fig. 18. Distributions of $\sigma_{VM}/E^*\bar{g}_r$ along the depth of the body for surfaces with kurtosis (a) $G(\mathbf{r})$: $\lambda_s = L_x/128$ and (b) $K_2(\mathbf{r})$: $\lambda_s = L_x/512$. $\lambda_{sn} = L_x/128$.

distributions are represented in Fig. 16a together with the original Gaussian distribution. In Fig. 16b the Gaussian distribution is instead shown together with two distributions with various kurtosis, obtained by varying the small wavelength of the surface spectrum. The surface indicated with $K_1(\mathbf{r})$ has $\lambda_s = L_x/64$, the surface $K_2(\mathbf{r})$ has $\lambda_s = L_x/512$.

When comparing the two skewed distribution in Fig. 17a it is possible to see that the positively skewed induces normalized Von-Mises stress peaks with larger magnitude, compared to the negatively skewed. This is because the positively skewed distribution corresponds to blunter hills and sharper valleys on the indenter surface. Here, we call hills the parts of the surface that first enter into contact with the substrate. Given that the contact area fraction reached in these simulations is only 10%, what happens to the valleys is irrelevant. Notice that trend observed in the figure is a consequence of the normalization of the distribution on the rms gradient, which is significantly lower for positively skewed surface. Without normalizing on the rms gradient the Von Mises stress peaks would be smallest for the positively skewed surface height distribution. As seen from Fig. 17b, increasing the kurtosis by including smaller wavelength in the description of the surface induces Von Mises stresses with larger magnitudes and broader distribution. Additionally, by including smaller wavelengths the high stress concentrations occur closer to the interface, as shown in Fig. 18.

6. Conclusions

This work focusses on two aspects that have, in our opinion, received too little attention from the contact mechanics community: the subsurface stresses induced by contact between rough surfaces and the effect of compressibility of the bodies on those stresses. When two solids are brought into frictionless contact, although the interface experiences only normal displacement, the stress tensor induced in the body can have non-zero stress components in directions normal to the loading. These stress components need to be considered if one wants to calculate the Von Mises stress acting in the body, since they cannot in general be inferred from the normal stress fields. In this work we have first extended the Green's function molecular dynamics technique to address contact between compressible finite elastic bodies in three-dimensions. Next, we have analysed the local subsurface Von Mises stress peaks induced by contact between a flat solid with various compressibility and a rough rigid surface with different Hurst exponent. Results show that for a given contact roughness the larger is the compressibility of the substrate, the smaller is the stress normal to the loading direction, and thus the higher are the Von Mises stress peaks: a factor of 1.5 between zero and maximum compressibility. This entails that the compressible bodies will deform plastically at a lower applied load when in contact with a rough surface. The decay of the stress peaks in the bodies is negligibly affected by compressibility.

While surfaces with different Hurst exponent induce a distribution of contact traction peaks that scales with the rms gradient, the same scaling does not hold for the subsurface Von Mises stress peaks, because those are also affected by the shear stresses in the body, which scale differently. The shear stresses are however rather small compared to the normal stresses, so their effect does not change the Von Mises stress very much. The decay of the stress peaks is slower when the Hurst exponent is large. This entails that there are larger regions in the subsurface where the Von Mises stress reaches large values. It is expected that bodies where plasticity is size dependent are more likely to deform plastically when the Hurst exponent is large.

When considering indenters with skewed height distribution, we find that the induced Von-Mises stresses have smaller magnitude if the skeweness is positive, because the surface roughness is blunter at its hills and has a small rms gradient compared to the negatively skewed. Increasing the kurtosis of the distribution by including smaller wavelength has the effect of increasing the magnitude and breadth of the subsurface Von Mises stress peaks and moving the peaks closer to the interface.

CRediT authorship contribution statement

Yaswanth Murugesan: Conceptualization, Methodology, Software, Validation, Formal analysis, Investigation, Data curation, Writing – original draft. **Syam P. Venugopalan:** Conceptualization, Methodology, Software, Supervision. **Lucia Nicola:** Conceptualization, Methodology, Resources, Writing – review & editing, Visualization, Supervision, Project administration, Funding acquisition.

Declaration of competing interest

The authors declare that they have no known competing financial interests or personal relationships that could have appeared to influence the work reported in this paper.

Acknowledgement

LN received funding from the European Research Council (ERC) under the European Union's Horizon 2020 research and innovation programme (grant agreement no. 681813).

Appendix A. Green's function tensor

The surface displacement is related to the traction via Green's function tensor $[\widetilde{G}_{ij}(\mathbf{q})]$ read as:

$$\begin{bmatrix} \widetilde{u}_x(\mathbf{q}, z_\mathrm{m}) \\ \widetilde{u}_y(\mathbf{q}, z_\mathrm{m}) \\ \widetilde{u}_z(\mathbf{q}, z_\mathrm{m}) \\ \widetilde{u}_x(\mathbf{q}, z_0) \\ \widetilde{u}_y(\mathbf{q}, z_0) \\ \widetilde{u}_z(\mathbf{q}, z_0) \end{bmatrix} = \left[\widetilde{G}_{ij}(\mathbf{q})\right] \begin{bmatrix} \widetilde{t}_x(\mathbf{q}, z_\mathrm{m}) \\ \widetilde{t}_y(\mathbf{q}, z_\mathrm{m}) \\ \widetilde{t}_z(\mathbf{q}, z_\mathrm{m}) \\ \widetilde{t}_x(\mathbf{q}, z_0) \\ \widetilde{t}_y(\mathbf{q}, z_0) \\ \widetilde{t}_z(\mathbf{q}, z_0) \end{bmatrix}, \tag{A.1}$$

with

$$\left[\widetilde{G}_{ij}(\mathbf{q})\right] = \begin{bmatrix} \widetilde{G}_{11}(\mathbf{q}) & \widetilde{G}_{12}(\mathbf{q}) & i\widetilde{G}_{13}(\mathbf{q}) & \widetilde{G}_{14}(\mathbf{q}) & \widetilde{G}_{15}(\mathbf{q}) & i\widetilde{G}_{16}(\mathbf{q}) \\ \widetilde{G}_{12}(\mathbf{q}) & \widetilde{G}_{22}(\mathbf{q}) & i\widetilde{G}_{23}(\mathbf{q}) & \widetilde{G}_{15}(\mathbf{q}) & \widetilde{G}_{25}(\mathbf{q}) & i\widetilde{G}_{26}(\mathbf{q}) \\ -i\widetilde{G}_{13}(\mathbf{q}) & -i\widetilde{G}_{23}(\mathbf{q}) & \widetilde{G}_{33}(\mathbf{q}) & i\widetilde{G}_{16}(\mathbf{q}) & i\widetilde{G}_{26}(\mathbf{q}) & \widetilde{G}_{36}(\mathbf{q}) \\ \widetilde{G}_{14}(\mathbf{q}) & \widetilde{G}_{15}(\mathbf{q}) & -i\widetilde{G}_{16}(\mathbf{q}) & \widetilde{G}_{11}(\mathbf{q}) & \widetilde{G}_{12}(\mathbf{q}) & -i\widetilde{G}_{13}(\mathbf{q}) \\ \widetilde{G}_{15}(\mathbf{q}) & \widetilde{G}_{25}(\mathbf{q}) & -i\widetilde{G}_{26}(\mathbf{q}) & \widetilde{G}_{12}(\mathbf{q}) & \widetilde{G}_{22}(\mathbf{q}) & -i\widetilde{G}_{23}(\mathbf{q}) \\ -i\widetilde{G}_{16}(\mathbf{q}) & -i\widetilde{G}_{26}(\mathbf{q}) & \widetilde{G}_{36}(\mathbf{q}) & i\widetilde{G}_{13}(\mathbf{q}) & i\widetilde{G}_{23}(\mathbf{q}) & \widetilde{G}_{33}(\mathbf{q}) \end{bmatrix}. \tag{A.2}$$

The elements of the Green's function tensor assuming $z_0 = 0$ are:

$$\widetilde{G}_{11}(q)=\frac{-8e^{3z_m q_r}\left(1+\nu\right)\sinh\left(q_r z_m\right)\left[q_y^2 q_r\left(-2q_y^2 z_m^2\coth\left(q_r z_m\right)+\sinh\left(2q_r z_m\right)\right)\right]}{\left(-1+e^{2z_m q_r}\right)^3 E q_r^4\left[-1+q_r^2 z_m^2\operatorname{cosech}^2\left(q_r z_m\right)\right]}\frac{-8e^{3z_m q_r}\left(1+\nu\right)\sinh\left(q_r z_m\right)\left[2q_x^2 q_y^2 z_m\left(-1+\nu-q_r z_m\coth\left(q_r z_m\right)\right)\right]}{\left(-1+e^{2z_m q_r}\right)^3 E q_r^4\left[-1+q_r^2 z_m^2\operatorname{cosech}^2\left(q_r z_m\right)\right]}\frac{-8e^{3z_m q_r}(1+\nu)\sinh\left(q_r z_m\right)\left[2(\nu-1)z_m q_x^4+q_x^2(1-\nu)q_r\sinh\left(2q_r z_m\right)\right]}{\left(-1+e^{2z_m q_r}\right)^3 E q_r^4\left[-1+q_r^2 z_m^2\operatorname{cosech}^2\left(q_r z_m\right)\right]}$$

$$\widetilde{G}_{12}(q)=\frac{8e^{3z_m q_r}(\nu+1)\sinh^3(z_m q_r)q_x q_y\left[\coth(z_m q_r)\left(2\nu\sinh^2(z_m q_r)\right)q_r\right]}{\left(-1+e^{2z_m q_r}\right)^3 E q_r^4\left[z_m^2 q_r^2-\sinh^2(z_m q_r)\right]}+\frac{8e^{3z_m q_r}(\nu+1)\sinh^3(z_m q_r)q_x q_y\left[\coth(z_m q_r)\left(-2z_m^2 q_r^2\right)q_r\right]}{\left(-1+e^{2z_m q_r}\right)^3 E q_r^4\left[z_m^2 q_r^2-\sinh^2(z_m q_r)\right]}+\frac{8e^{3z_m q_r}(\nu+1)\sinh^3(z_m q_r)q_x q_y\left[-2z_m(\nu-1)q_r^2\right]}{\left(-1+e^{2z_m q_r}\right)^3 E q_r^4\left[z_m^2 q_r^2-\sinh^2(z_m q_r)\right]}$$

$$\widetilde{G}_{13}(q)=-\frac{(\nu+1)q_x\left[(2\nu-1)\sinh^2(z_m q_r)-z_m^2 q_r^2\right]}{E q_r^2\left[z_m^2 q_r^2-\sinh^2(z_m q_r)\right]}$$

$$\widetilde{G}_{22}(q)=\frac{8e^{3z_m q_r}\left(\nu+1\right)\sinh^3(z_m q_r)\left[-2z_m\left(\nu-1\right)q_r^2 q_y^2\right]}{\left(-1+e^{2z_m q_r}\right)^3 E q_r^4\left[z_m^2 q_r^2-\sinh^2(z_m q_r)\right]}+\frac{8e^{3z_m q_r}\left(\nu+1\right)\sinh^3(z_m q_r)\left[\sinh(2z_m q_r)\left(\left(\nu-1\right)q_y^2-q_x^2\right)q_r\right]}{\left(-1+e^{2z_m q_r}\right)^3 E q_r^4\left[z_m^2 q_r^2-\sinh^2(z_m q_r)\right]}+\frac{8e^{3z_m q_r}(\nu+1)\sinh^3(z_m q_r)\left[2z_m^2\coth(z_m q_r)q_x^2 q_r^3\right]}{\left(-1+e^{2z_m q_r}\right)^3 E q_r^4\left[z_m^2 q_r^2-\sinh^2(z_m q_r)\right]}$$

$$\widetilde{G}_{23}(q)=-\frac{(\nu+1)q_y\left[(2\nu-1)\sinh^2(z_m q_r)-z_m^2 q_r^2\right]}{E q_r^2\left[z_m^2 q_r^2-\sinh^2(z_m q_r)\right]}$$

$$\widetilde{G}_{33}(q)=\frac{(\nu^2-1)[\sinh(2z_m q_r)+2z_m q_r]}{E\sqrt{q_r^2}\left[z_m^2 q_r^2-\sinh^2(z_m q_r)\right]}$$

$$\widetilde{G}_{14}(q)=\frac{e^{z_m q_r}\left(\nu+1\right)(\coth(z_m q_r)-1)\left[2q_r\left(z_m^2 q_y^4-\sinh^2(z_m q_r)q_y^2\right)\right]}{E q_r^4\left(z_m^2 q_r^2-\sinh^2(z_m q_r)\right)}+\frac{e^{z_m q_r}\left(\nu+1\right)(\coth(z_m q_r)-1)\left[2q_r q_x^2\left(\left(\nu-1\right)\sinh^2(z_m q_r)+z_m^2 q_y^2\right)\right]}{E q_r^4\left(z_m^2 q_r^2-\sinh^2(z_m q_r)\right)}+\frac{e^{z_m q_r}(\nu+1)(\coth(z_m q_r)-1)\left[-z_m(\nu-1)\sinh(2z_m q_r)q_x^2 q_r^2\right]}{E q_r^4\left(z_m^2 q_r^2-\sinh^2(z_m q_r)\right)}$$

$$\widetilde{G}_{15}(q)=\frac{e^{-z_m q_r}(\nu+1)(\coth(z_m q_r)+1)q_x q_y\left[-z_m(\nu-1)\sinh(2z_m q_r)q_r^2\right]}{E q_r^4\left[z_m^2 q_r^2-\sinh^2(z_m q_r)\right]}+\frac{e^{-z_m q_r}(\nu+1)(\coth(z_m q_r)+1)q_x q_y\left[-2\left(z_m^2 q_r^2-\nu\sinh^2(z_m q_r)\right)q_r\right]}{E q_r^4\left[z_m^2 q_r^2-\sinh^2(z_m q_r)\right]}$$

$$\widetilde{G}_{16}(q)=\frac{4z_m\left(\nu^2-1\right)\sinh(z_m q_r)q_x}{E\sqrt{q_r^2}\left[-2z_m^2 q_r^2+\cosh(2z_m q_r)-1\right]}$$

$$\widetilde{G}_{25}(q)=\frac{2\left(\nu+1\right)\sinh(z_m q_r)\left[-z_m\left(\nu-1\right)\coth(z_m q_r)q_y^2 q_r\right]}{E\left(q_r^2\right)^{3/2}\left[z_m^2 q_r^2-\sinh^2(z_m q_r)\right]}+\frac{2\left(\nu+1\right)\sinh(z_m q_r)\left[\left(z_m^2\operatorname{cosech}^2(z_m q_r)q_r^2-1\right)q_x^2+\left(\nu-1\right)q_y^2\right]}{E\left(q_r^2\right)^{3/2}\left[z_m^2 q_r^2-\sinh^2(z_m q_r)\right]}$$

$$\widetilde{G}_{26}(q)=\frac{4z_m\left(\nu^2-1\right)\sinh(z_m q_r)q_y}{E\sqrt{q_r^2}\left[-2z_m^2 q_r^2+\cosh(2z_m q_r)-1\right]}$$

$$\widetilde{G}_{36}(q)=\frac{2(\nu^2-1)[\sinh(z_m q_r)+z_m\cosh(z_m q_r)q_r]}{E\sqrt{q_r^2}\left[z_m^2 q_r^2-\sinh^2(z_m q_r)\right]}$$

(A.3)

References

[1] Bush A, Gibson R, Thomas T. The elastic contact of a rough surface. Wear 1975;35:87–111. https://doi.org/10.1016/0043-1648(75)90145-3.

[2] Greenwood JA, Williamson JBP, Bowden FP. Contact of nominally flat surfaces. Proc Roy Soc Lond Math Phys Sci 1966;295:300–19. https://doi.org/10.1098/rspa.1966.0242.

[3] Greenwood J. A simplified elliptic model of rough surface contact. Wear 2006;261:191–200. https://doi.org/10.1016/j.wear.2005.09.031.

[4] Ciavarella M, Delfine V, Demelio G. A "re-vitalized" greenwood and williamson model of elastic contact between fractal surfaces. J Mech Phys Solid 2006;54:2569–91. https://doi.org/10.1016/j.jmps.2006.05.006.

[5] Persson B. Adhesion between an elastic body and a randomly rough hard surface. Eur Phys J 2002;8:385–401. https://doi.org/10.1140/epje/i2002-10025-1.

[6] Campañá C, Müser MH. Practical green's function approach to the simulation of elastic semi-infinite solids. Phys Rev B 2006;74:075420. https://doi.org/10.1103/PhysRevB.74.075420.

[7] Prodanov N, Dapp WB, Müser MH. On the contact area and mean gap of rough, elastic contacts: dimensional analysis, numerical corrections, and reference data. Tribol Lett 2014;53:433–48. https://doi.org/10.1007/s11249-013-0282-z.

[8] Putignano C, Dapp WB, Müser MH. A green's function molecular dynamics approach to the mechanical contact between thin elastic sheets and randomly rough surfaces. Biomimetics 2016;1:1–7. https://doi.org/10.3390/biomimetics1010007.

[9] Polonsky I, Keer L. A numerical method for solving rough contact problems based on the multi-level multi-summation and conjugate gradient techniques. Wear 1999;231:206–19. https://doi.org/10.1016/S0043-1648(99)00113-1.

[10] Stanley HM, Kato T. An fft-based method for rough surface contacts. J Tribol 1997;119:481–5. https://doi.org/10.1115/1.2833523.

[11] Wu J-J. Numerical analyses on elliptical adhesive contact. J Phys Appl Phys 2006;39:1899–907. https://doi.org/10.1088/0022-3727/39/9/027.

[12] Hyun S, Pei L, Molinari J-F, Robbins MO. Finite-element analysis of contact between elastic self-affine surfaces. Phys Rev E 2004;70:026117. https://doi.org/10.1103/PhysRevE.70.026117.

[13] Hyun S, Robbins MO. Elastic contact between rough surfaces: effect of roughness at large and small wavelengths. Tribol Int 2007;40:1413–22. https://doi.org/10.1016/j.triboint.2007.02.003.

[14] Dapp WB, Prodanov N, Müser MH. Systematic analysis of persson's contact mechanics theory of randomly rough elastic surfaces. J Phys Condens Matter 2014;26:355002. https://doi.org/10.1088/0953-8984/26/35/355002.

[15] Putignano C, Dapp WB, Müser MH. A green's function molecular dynamics approach to the mechanical contact between thin elastic sheets and randomly rough surfaces. Biomimetics 2016;1:1–7. https://doi.org/10.3390/biomimetics1010007.

[16] Venugopalan SP, Müser MH, Nicola L. Green's function molecular dynamics meets discrete dislocation plasticity. Model Simulat Mater Sci Eng 2017;25:065018. https://doi.org/10.1088/1361-651X/aa7e0e.

[17] Dokkum JSV, Nicola L. Green's function molecular dynamics including viscoelasticity. Model Simulat Mater Sci Eng 2019;27:075006. https://doi.org/10.1088/1361-651X/ab3031.

[18] Müser M, Dapp W, Bugnicourt R, Sainsot P, Lesaffre N, Lubrecht T, Persson B, Harris K, Bennett A, Schulze K, Rohde S, Ifju P, Angelini T, Esfahani H, Kadkhodaei M, Akbarzadeh S, Wu J-J, Vorlaufer G, Greenwood J. Meeting the contact-mechanics challenge. Tribol Lett 2017;65:118. https://doi.org/10.1007/s11249-017-0900-2.

[19] Müser MH. Internal, elastic stresses below randomly rough contacts. J Mech Phys Solid 2018;119:73–82. https://doi.org/10.1016/j.jmps.2018.06.012.

[20] Venugopalan SP, Müser MH, Nicola L. Green's function molecular dynamics: including finite heights, shear, and body fields. Model Simulat Mater Sci Eng 2017;25:034001. https://doi.org/10.1088/1361-651X/aa606b.

[21] Sadd MH. Elasticity: theory, applications and numerics. second ed. ed. Boston: Academic Press; 2009. https://doi.org/10.1016/B978-0-12-374446-3.50002-9.

[22] Fischer-Cripps AC. Introduction to contact mechanics. second ed. New York, NY: Springer US; 2007. https://doi.org/10.1007/978-0-387-68188-7.

[23] Box GEP, Muller ME. A note on the generation of random normal deviates. Ann Math Stat 1958;29:610–1. https://doi.org/10.1214/aoms/1177706645.

[24] Nayak P. Random process model of rough surfaces in plastic contact. Wear 1973;26:305–33. https://doi.org/10.1115/1.3451608.

[25] David WJ. Handbook of surface and nanometrology. second ed. ed. Boca Raton: CRC Press; 2010. https://doi.org/10.1201/b10415.

[26] Horváth R, Czifra r, Drégelyi-Kiss g. Effect of conventional and non-conventional tool geometries to skewness and kurtosis of surface roughness in case of fine turning of aluminium alloys with diamond tools. Int J Adv Manuf Technol 2015;78:297–304. https://doi.org/10.1007/s00170-014-6642-5.

[27] D'Urso G, Giardini C, Quarto M. Characterization of surfaces obtained by micro-edm milling on steel and ceramic components. Int J Adv Manuf Technol 2018;97:2077–85. https://doi.org/10.1007/s00170-018-1962-5.

[28] Liu C, Gao L, Wang G, Xu W, Jiang X, Yang T. Online reconstruction of surface topography along the entire cutting path in peripheral milling. Int J Mech Sci 2020;185:105885. https://doi.org/10.1016/j.ijmecsci.2020.105885.

[29] Hafner R, Grguraš D, Kramar D. Milling process optimization for the best surface coat adhesion of the rigid polyurethane foam. J Polym Eng 2018;38:995–1005. https://doi.org/10.1515/polyeng-2018-0035.

[30] Duboust N, Ghadbeigi H, Pinna C, Ayvar-Soberanis S, Collis A, Scaife R, Kerrigan K. An optical method for measuring surface roughness of machined carbon fibre-reinforced plastic composites. J Compos Mater 2017;51:289–302. https://doi.org/10.1177/0021998316644849.

[31] Johnson NL. Systems of frequency curves generated by methods of translation. Biometrika 1949;36:149–76. https://doi.org/10.2307/2332539.